Strain Rate Imaging Using Two-Dimensional Speckle Tracking

K. Kaluzynski, Xunchang Chen, Stanislav Y. Emelianov, *Member, IEEE*, Andrei R. Skovoroda, and Matthew O'Donnell, *Fellow, IEEE*

Abstract—**Strain rate images (SRI) of the beating heart have been proposed to identify non-contracting regions of myocardium. Initial attempts used spatial derivatives of tissue velocity (Doppler) signals. Here, an alternate method is proposed based on two-dimensional phase-sensitive speckle tracking applied to very high frame rate, real-time images. This processing can produce high resolution maps of the time derivative of the strain magnitude (i.e., square root of the strain intensity). Such images complement traditional tissue velocity images (TVI), providing a more complete description of cardiac mechanics. To test the proposed approach, SRI were both simulated and measured on a thick-walled, cylindrical, tissue-equivalent phantom modeling cardiac deformations. Real-time ultrasound images were captured during periodic phantom deformation, where the period was matched to the data capture rate of a commercial scanner mimicking high frame rate imaging of the heart. Simulation results show that SRI with spatial resolution between 1 and 2 mm are possible with an array system operating at 5 MHz. Moreover, these images are virtually free of angle-dependent artifacts present in TVI and simple strain rate maps derived from these images. Measured results clearly show that phantom regions of low deformation, which are difficult to identify on tissue velocity-derived SRI, are readily apparent with SRI generated from two-dimensional phase-sensitive speckle tracking.**

I. Introduction

TVI, SOMETIMES called tissue Doppler imaging, was introduced by McDicken *et al.* in 1992 [1] and was further developed by Sutherland *et al.* in 1994 [2]. This technique uses conventional Doppler methods to track heart wall motion. Velocities in the cardiac wall are considerably lower (0 to 150 mm/s) than in the blood, but the echo amplitude is considerably higher than that of blood, making the technique very sensitive to small velocity components. Also, imaging parameters, such as the pulse repetition rate for Doppler estimates, are optimized for this velocity range and echo amplitude. Similar to color flow displays, TVI information is color-coded and superimposed on the B-Scan to produce a real-time image correlating the instantaneous tissue velocity distribution with cardiac anatomy.

One difficulty associated with TVI is that it does not differentiate between active contraction (i.e., deformation) and simple translation or rotation of the heart wall. To overcome this problem, Fleming *et al.* suggested using the spatial gradient of the TVI velocity to measure the relative change in wall thickness [3]. Several groups have actively pursued this concept using measurements of the local variation in Doppler velocity, or

$$\dot{\varepsilon} = \frac{\partial v(r)}{\partial r}, \tag{1}$$

which can be estimated by

$$\dot{\varepsilon} = \frac{v(r+\Delta r) - v(r)}{\Delta r} \tag{2}$$

for small increments in r [4]–[7]. Here, v is the local velocity along the ultrasonic propagation direction, ε is the axial normal strain, and r is the direction along the acoustic beam axis. By applying this technique, the local velocity is determined employing usual Doppler methods. Adjacent, axial estimates of the tissue velocity are subtracted to get the velocity gradient along the ultrasound beam. Much as with TVI, applications of SRI have involved mainly the left ventricle [8]–[9].

Although both TVI and SRI have the potential to map contractile processes through and along the myocardial wall, they are limited in general utility because they present angle-dependent estimates of wall velocity and deformation rate [10]–[11]. Angle dependency is a significant problem that must be minimized to realize the full potential of TVI and SRI.

Current TVI and SRI sequences use two or more pulses per beam, where the interval between firings is typically about 1 to 2 ms. This interval matches Doppler processing parameters to expected peak tissue velocities. For example, typical tissue velocities peak at about 150 mm/s, producing a maximum displacement of about 0.15 mm in 1 ms. This creates a 2π phase shift in the Doppler signal at a carrier frequency of 5.0 MHz or a π phase shift at a 2.5-MHz carrier. Phase shifts much greater than 2π are hard to unwrap (e.g., a 2π phase shift aliases to 0 phase shift); so, displacements greater than this are a significant problem for TVI and SRI systems based on Doppler processing. For a 1-ms pulse interval, the deformation reaches a peak magnitude of about 0.2%, assuming a maximum strain rate of

Manuscript received September 12, 2000; accepted February 27, 2001. K. Kaluzynski gratefully acknowledges the support of the Dekaban Fund and the University of Michigan. This project was also supported in part by NIH grants DK47324 and HL47401.

K. Kaluzynski is with the Institute for Precision and Biomedical Engineering, Warsaw University of Technology, 02-525 Warsaw, Poland.

X. Chen, S. Y. Emelianov, and M. O'Donnell are with the Biomedical Engineering Department, University of Michigan, Ann Arbor, MI 48109-2125 (e-mail: odonnel@umich.edu).

A. R. Skovoroda is with the Institute of Mathematical Problems of Biology, Russian Academy of Sciences, Pushchino, Moscow Region, Russia 142292.

2.0 s^{-1}. This is a very low deformation magnitude, and, consequently, spatial resolution must be greatly sacrificed to provide adequate signal to noise ratio (SNR) SRI.

We propose an alternate method using much longer firing intervals. An inter-firing interval of about 5 to 10 ms should produce peak displacements of about 0.75 to 1.5 mm and peak strain magnitudes of about 1 to 2%. Both high spatial resolution and high SNR SRI and TVI can be produced with this level of deformation using two-dimensional phase-sensitive speckle tracking algorithms specifically designed for this displacement and deformation range [12]–[16]. For full two-dimensional speckle tracking, however, the entire image, or a significant subimage, must be produced within the firing interval. This necessitates frame rates greater than 200 Hz for typical adult cardiac applications.

High frame rate ultrasound imaging is a continuing topic of research interest [17]–[29]. Frame rates greater than 200 Hz are available on some clinical systems. With renewed interest in understanding cardiac dynamics, higher quality, high frame rate images should become available on commercial systems in the very near future. Consequently, SRI methods relying on conventional imaging at frame rates exceeding 200 Hz should be clinically viable in the very near future, enabling comparisons between SRI methods based on full two-dimensional phase-sensitive speckle tracking and those based on tissue Doppler measurements.

In Section II, we describe an SRI method building on previous two-dimensional phase-sensitive speckle tracking work in our laboratory. Results of simulations and measurements on a simple tissue-equivalent phantom mimicking cardiac deformations are presented in Section III. These results, as well as comparisons with current SRI methods, are discussed in Section IV.

II. Methods

The ventricular walls of the heart are deformed by internal forces within the myocardium itself. In turn, these deformations pressurize the ventricle to produce the pumping action of the heart. By inverting the process, ventricular wall deformations can be modeled with a passive mechanical medium. For example, consider a thick-walled, elastically homogeneous, spherical shell with a fluid-filled inner chamber. If the incompressible fluid is pressurized, then the wall will deform in a very similar way to deformations created by uniform internal wall forces producing the equivalent chamber pressure. Thus, mechanical characterization of a closed, active system can be modeled with a closed, passive system under internal pressure.

We approximated a closed, passive system under pressure using a long, thick-walled cylindrical tube with an incompressible fluid in the lumen. In the limit of infinite length, the tube cross section can be considered a closed mechanical system with an inner pressurized fluid chamber. As the lumen pressure changes, the wall moves as if internal forces were deforming the medium until the same pressure change was produced in the lumen. We used this simple mechanical model to test new SRI algorithms.

For the studies presented here, the object was assumed to be an infinitely long, thick-walled cylindrical tube within an annular cross section of 9.2-mm inner diameter and 31-mm outer diameter, with uniform elastic modulus throughout the wall and an incompressible fluid filling the tube lumen. For a homogeneous annulus under uniform pressure from the lumen, a simple two-dimensional model of incompressible deformation predicts that the internal lateral and axial displacements are

$$u = K r_0 \frac{x}{r^2} \text{ and} \tag{3}$$

$$v = K r_0 \frac{y}{r^2} \tag{4}$$

where u is the lateral displacement, v is the axial displacement, x is the lateral coordinate, y is the axial coordinate, r_0 is the undeformed lumen radius, r is the distance from the center of the tube lumen to a position within the wall, and K is proportional to the ratio of the lumen pressure to the wall's modulus (i.e., shear modulus).

For any mechanical system, the deformation magnitude is given by the strain magnitude (or strain intensity), a quantity independent of the choice of coordinate system. For a two-dimensional, incompressible system, the strain magnitude is defined as:

$$|\varepsilon| = \sqrt{\varepsilon_{22}^2 + \varepsilon_{12}^2} \tag{5}$$

where $\varepsilon_{22} = \partial v/\partial y$ is the axial normal strain and $\varepsilon_{12} = \frac{1}{2}(\partial v/\partial x + \partial u/\partial y)$ is the shear strain. In simple systems, such as the circularly symmetric one defined previously, the strain magnitude can be approximated using a single component of the displacement vector. In particular, the magnitude of the gradient of one displacement component (e.g., $|\nabla v|$) is often used in experimental systems in which only that component of the displacement vector can be measured.

For the system described by (3)–(4), the magnitude of the gradient of either displacement component equals the strain magnitude; that is,

$$|\varepsilon| = \sqrt{\varepsilon_{22}^2 + \varepsilon_{12}^2} = |\nabla u| = |\nabla v|. \tag{6}$$

This simple system, therefore, is a good test of strain magnitude images based on two-dimensional phase-sensitive speckle tracking because equivalent images can be computed directly from one-dimensional displacement estimates. That is, $|\varepsilon|$ images can be compared with $|\nabla v|$ images to judge errors introduced by a full two-dimensional search. It should be noted, however, that, for more complex mechanical systems, $|\varepsilon|$ images will capture the true magnitude of the deformation field, whereas $|\nabla v|$ images will be sensitive to system geometry.

For the results presented subsequently, two components of the displacement vector (u, v) were estimated using the

$$\rho'_{nm}(k,l) = \frac{\sum_{i=-K/2}^{i=K/2}\sum_{j=-L/2}^{j=L/2} W_{ij}\left[x(n+i,m+j)y^*(n+k+i,m+1+j)\right]}{\left[\sum_{i=-K/2}^{i=K/2}\sum_{j=-L/2}^{j=L/2} W_{ij}\left|x(n+i,m+j)\right|^2\right]^{1/2}\left[\sum_{i=-K/2}^{i=K/2}\sum_{j=-L/2}^{j=L/2} W_{ij}\left|y(n+k+i,m+1+j)\right|^2\right]^{1/2}}. \quad (7)$$

two-dimensional, phase-sensitive speckle tracking procedure described in [12]–[16]. Briefly, at every pixel in the initial phase-sensitive image (i.e., complex baseband or analytic signal representation), a two-dimensional correlation kernel of spatial extent, equaling approximately one speckle, is defined around the pixel. A speckle is defined as the full-width at half maximum in both dimensions of the two-dimensional autocorrelation function of the initial complex image. This kernel is then cross-correlated with the complex image following deformation. The resultant cross-correlation coefficient $\rho'_{nm}(k,l)$ at pixel (n,m) as a function of lags (k,l) is (7) (see above). In this expression, $x(n,m)$ is the original complex image, $y(n,m)$ is the post-deformation image, and W_{ij} is a simple two-dimensional weighting function over the $2K+1 \times 2L+1$ point correlation kernel. The correlation coefficient is a unit-normalized, complex function of lags (k,l). To improve SNR, it is then filtered with a unity gain function ($\sum F_{ij} = 1$) defined over a $2I+1 \times 2J+1$ point region of support:

$$\rho_{nm}(k,l) = \sum_{i=-I/2}^{i=I/2}\sum_{j=-J/2}^{j=J/2} F_{ij}\left[\rho'_{n+i\,m+j}(k,l)\right]. \quad (8)$$

Following filtering, the two-dimensional coordinates of the correlation peak position are computed at every pixel to estimate the two-dimensional displacement vector $(u(n,m), v(n,m))$. The displacement is computed in two steps. First, the peak position is estimated via conventional two-dimensional interpolation. Then, the axial displacement (i.e., v) estimate is refined using the position of the closest zero-crossing of the phase of the complex correlation function. This processing produces three output images: $u(n,m)$, $v(n,m)$, and the magnitude of the correlation coefficient, $|\rho(n,m)|$. Details of this procedure are presented in [12]–[16].

Because of the limited spatial frequencies available from a finite imaging aperture, lateral displacement estimates are much noisier than axial ones. Errors in the lateral displacement can be greatly reduced using incompressibility processing as discussed in [30], [31]. Briefly, by assuming that the deformed medium is incompressible, a reasonable assumption for soft tissue, the normal components of the strain tensor are not independent. Incompressibility requires that the two normal spatial derivatives of the displacement components be opposite in sign and equal in magnitude, that is,

$$\varepsilon_{11} + \varepsilon_{22} = 0 \rightarrow \frac{\partial v}{\partial y} = -\frac{\partial u}{\partial x}. \quad (9)$$

This principle can be exploited to develop a filtering method using both components of the displacement vector to greatly reduce errors in lateral displacement estimates for a very minor price in spatial resolution. Details of this procedure are presented in [30], [31].

A. Simulations

To investigate ultrasound images of a thick-walled annulus under deformation, a computer simulation of a two-dimensional, real-time, linear array system was created using methods similar to those previously developed in our lab [32]–[34]. A linear array geometry was chosen to approximate the experimental system described subsequently. The active aperture on every beam line was 18 mm, similar to the aperture available for adult cardiac imaging. The operating frequency was 5 MHz, the fractional bandwidth was 50%, and the pulse envelope was Gaussian. Each image frame was formed from 128 equally spaced beams over a 40-mm wide rectilinear scan space, where RF data on each beam were sampled at 20 MHz.

Identical point scatterers were randomly distributed within the annular wall, with a 15-μm mean distance between scatterers. This distribution well modeled a fully developed speckle source. The two-dimensional, phase-sensitive point response from each scatterer was computed, and the resultants were summed to produce a frame of RF data.

The center of the annulus was positioned 80 mm from the transducer surface, corresponding to an f/number of 4.44 to the center of the scattering object. This is a typical value for many cardiac applications operating at 5 MHz. For optimal performance, the imaging system was assumed to be dynamically focused on both transmit and receive (i.e., fully confocal system). This is a slight oversimplification of a real system using a fixed focus on transmit and dynamic focusing only on receive. However, for the f/numbers assumed here, this simplification reasonably approximates a clinical system. A B-scan of the simulated phantom is presented in Fig. 1 over a 40-dB display dynamic range. This image and all subsequent simulation images represent an area of 40 mm $\times$ 40 mm.

Images of the phantom were produced in undeformed and deformed states. The undeformed image was created with scatterers in their original positions (Fig. 1). The lumen was then pressurized, and the internal scatterers were moved from their original positions according to (3)–(4). The imaging model was applied to this new distribution to produce a second frame of RF data.

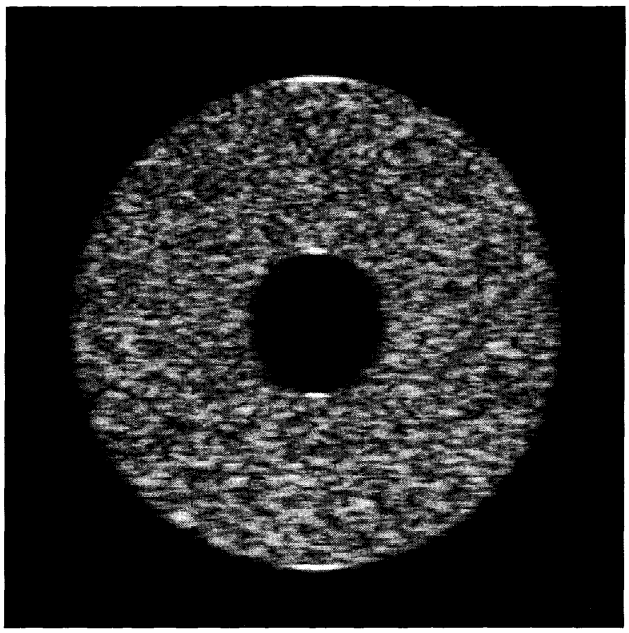

Fig. 1. B-Scan image displayed over a 40-dB display dynamic range of simulated thick-walled annulus. The inner diameter of the annulus is 9.2 mm, the outer diameter is 31 mm, and the total display area is 40 mm × 40 mm.

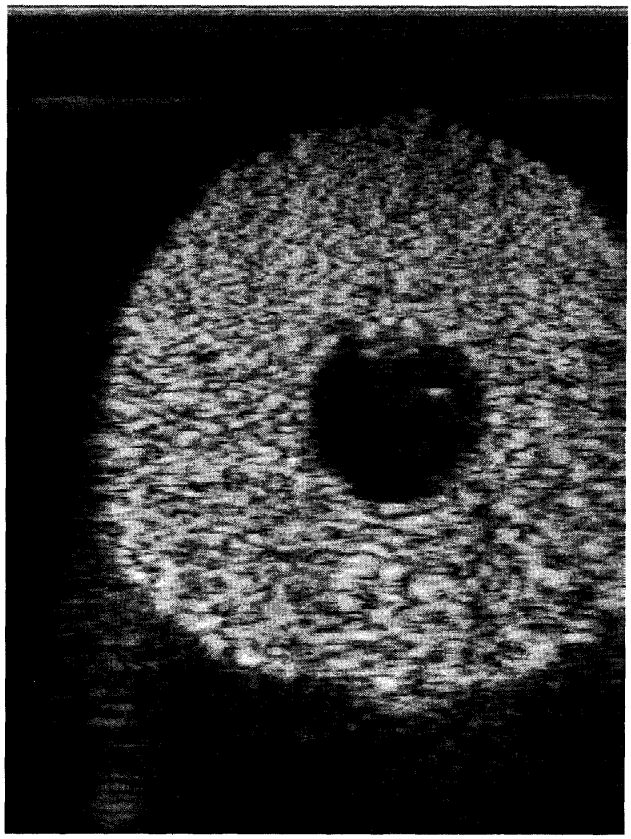

Fig. 2. B-Scan image displayed over a 40-dB display dynamic range of thick-walled, cylindrical rubber phantom. The inner diameter of the annular cross-section is 9.2 mm, the outer diameter is 31 mm, and the total display area is 38 mm × 50 mm.

These two frames were then processed with the two-dimensional phase-sensitive speckle tracking procedures described previously. The correlation kernel was approximately 0.5 mm axially × 0.75 mm laterally, and a small correlation filter was applied to produce spatial maps of the axial displacement, the lateral displacement, and the magnitude of the correlation coefficient. The spatial resolution of displacement and correlation coefficient images was estimated to be 0.8 mm axially × 2.0 mm laterally, corresponding to an average resolution of about 1.4 mm. We used discrete space approximations to spatial derivatives that preserved this resolution, producing displacement gradient and strain images with an average resolution of about 1.4 mm.

B. Measurements

A cylindrical rubber model seeded with 0.4% by weight polystyrene spheres (Analytical Grade Cation Exchange Resin, AG 50 W-X12, Bio-RAD Labs, Hercules, CA) with diameters ranging from 40 to 120 μm was constructed for the experiments. The phantom was 130 mm long, 31 mm in diameter, and had an inner lumen 9.2 mm in diameter. The lumen was connected to flow tubes at each end of the phantom to control internal pressure. This geometry closely approximated the thick-walled simulation model. In addition, however, a small "inclusion" about 2 mm thick, extending about 20 mm around the outer phantom circumference, was produced, where the shear modulus of the inclusion only differed from the background by about a factor of three as determined by independent mechanical measurements performed on the system described in [35].

The phantom was deformed by pumping water into the lumen with the outlet tube constricted. This pressurized the lumen. The outlet tube was subsequently released, allowing the phantom to return to its initial position. Real-time data were recorded during both phantom compression and expansion using a commercial ultrasonic scanner (ATL, Ultramark 9) adapted for RF data capture. All experiments were performed with a 38-mm linear array operating at 5 MHz with the center of the lumen positioned approximately 30 mm from the transducer surface to place the entire phantom within the elevational lens' depth of field.

Overall timing of the experiment was controlled so that approximately 166 frames were recorded over a single deformation cycle. That is, this system emulated a high speed scanner operating at a 200-Hz frame rate and imaging a heart beating at a rate of about 72 bpm. A B-scan of the phantom at one position in the cycle is presented in Fig. 2 over a 40-dB display dynamic range. This image and all subsequent experimental images represent an area of approximately 38 mm by 50 mm. The pressure was controlled so that average strain magnitudes (relative to the initial

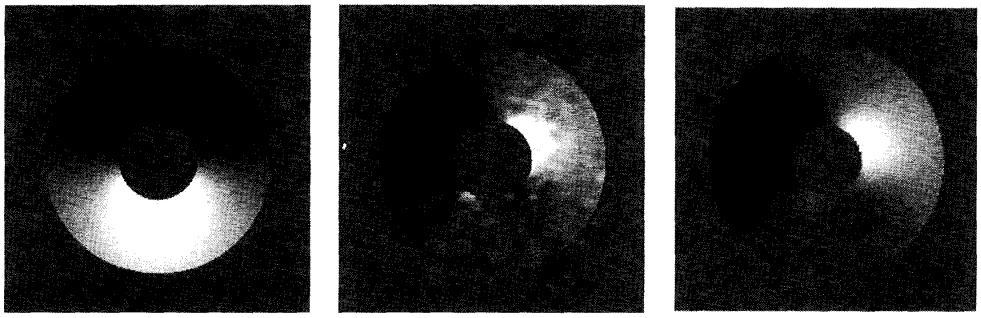

Fig. 3. Displacements estimated in a simulated annular phantom for a 135-μm radial displacement at the lumen boundary. a) Axial displacement, where white represents a downward displacement of 50 μm and black represents an upward displacement of 50 μm; b) lateral displacement, where white represents a rightward displacement of 50 μm and black represents a leftward displacement of 50 μm, and c) lateral displacement resulting from incompressibility processing of panel (b) based on the axial displacement of panel (a) using the same gray scale as panel (b).

position) were less than 20%, and peak strain rates were about 2.0 s^{-1}, close to normal values in the heart [6].

All experimental results presented subsequently used precisely the same two-dimensional phase-sensitive speckle tracking algorithms as the simulation studies. Because the size of the lateral point spread function close to the transducer surface is slightly bigger than that assumed in the simulation, the correlation kernel was slightly increased to 0.5 mm axially $\times$ 1.0 mm laterally. The correlation filter dimension was also increased to produce displacement and correlation coefficient images with a spatial resolution of approximately 1.25 mm axially $\times$ 2.25 mm laterally, corresponding to an average spatial resolution of about 1.75 mm. Again, we used discrete space approximations to spatial derivatives that preserved this resolution, producing displacement gradient and strain images with an average resolution of about 1.75 mm. Spatial derivatives of lateral displacement images produced by incompressibility processing were further spatially smoothed to produce high SNR shear strain images but with a degraded spatial resolution of about 2.0 mm. Interframe displacements and strains were frame-averaged over a running window representing a 50-ms interval assuming a 200-Hz frame rate. This processing temporally smoothes the deformation pattern but does not produce tracking artifacts because all correlations are performed from frame to frame.

III. Results

A. Simulations

The applied luminal pressure produced a peak radial displacement of about 130 μm and a peak radial deformation at the lumen surface of about 2.8%. The resulting axial displacement estimated from two-dimensional phase-sensitive speckle tracking is presented in Fig. 3(a) over a display dynamic range from -50 μm (black) to 50 μm (white), where a plus sign corresponds to motion away from the transducer (down), a minus sign represents motion toward the transducer (up), and mid gray represents no motion. In this image and all subsequent images, displacement and strain maps are masked using the corresponding B-scan, similar to conventional color-flow processing. The masked region is displayed as mid gray, unless deformation information is overlaid on the B-scan. Note that the axial displacement near 3 o'clock, and 9 o'clock is nearly zero, even though there is significant radial displacement in these regions.

The estimated lateral displacement over precisely the same display dynamic range is presented in Fig. 3(b), where a plus sign corresponds to motion to the right and a minus sign represents motion to the left. As expected, the lateral displacement is significantly noisier than the axial (i.e., higher error for tracking across the beam direction). The result of incompressibility processing using both axial and lateral displacement estimates produces the lateral displacement map of Fig. 3(c). Note the higher SNR for this image [Fig. 3(c)] compared with that produced directly by the speckle tracking procedure [Fig. 3(b)].

Fig. 4(a) presents the axial normal strain (i.e., the derivative of the axial displacement with respect to axial dimension) over a display dynamic range from -0.75% to 0.75%, representing a strain rate scale from about -1.0 to 1.0 s^{-1} assuming a frame rate of 133 Hz. In this image, black corresponds to compression, and white corresponds to expansion. Note that, at 3 o'clock and 9 o'clock, the strain image suggests expansion, whereas the material is actually compressing radially. This is a simple but powerful demonstration of potential angle-dependent problems in SRI. Even if the magnitude of the axial normal strain is displayed, there are still significant angle-dependent artifacts. Between 1 and 2 o'clock, 4 and 5 o'clock, 7 and 8 o'clock, and 10 and 11 o'clock, the axial normal strain is nearly zero, suggesting a non-deforming region.

Other components of the two-dimensional strain tensor can be computed to reduce angle-dependent artifacts in SRI. The lateral derivative of the axial displacement, representing one term in the shear strain, is presented in Fig. 4(b) over the same gray scale used for the axial normal strain in Fig. 4(a). Note that angle-dependent artifacts are different. The images in Fig. 4(a and b) represent the two components of the spatial gradient of the axial displace-

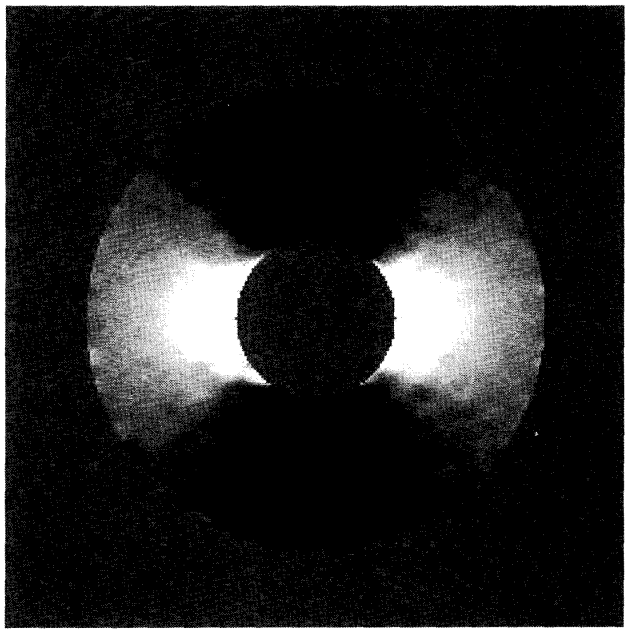

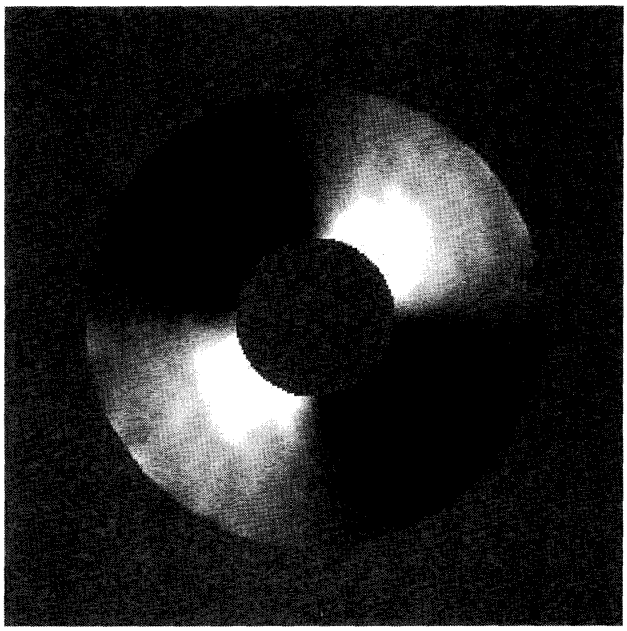

Fig. 4. Derivatives of the axial displacement in the simulated annular phantom for the same deformation as Fig. 3. a) Axial derivative (axial normal strain) displayed with a bipolar gray scale, where black represents a compression rate of 1.0 s^{-1} and white is an expansion rate of 1.0 s^{-1}; b) lateral derivative (one component of the shear strain) displayed over the same bipolar scale as (a).

ment. If either Fig. 4(a) or Fig. 4(b) alone is viewed as the total deformation map, significant misinterpretations will be made.

Nearly angle-independent deformation measures can be computed by combining all components of the strain tensor. As discussed in Section II, the strain magnitude represents a measure of deformation magnitude independent of the coordinate system. This means it is invariant to different scan geometries, such as sector scans versus linear scans. It does depend on the deformation geometry, but not the scan geometry. For the simple two-dimensional system presented here, the magnitude of the displacement gradient equals the strain magnitude. These two measures are compared in Fig. 5(a) ($|\nabla v|$) and Fig. 5(b) ($|\varepsilon|$). Both images exhibit the same spatial resolution, but the strain magnitude is slightly noisier than $|\nabla v|$. Angle-dependent artifacts have been greatly reduced using either parameter, although the strain magnitude exhibits a slight angular variation caused by decorrelation effects between 1 and 2 o'clock, 4 and 5 o'clock, 7 and 8 o'clock, and 10 and 11 o'clock. Overall, the quality of the $|\varepsilon|$ image rivals that of the $|\nabla v|$ image, even though noisy lateral displacement estimates were used to compute $|\varepsilon|$.

Other approximate measures of strain magnitude can help identify artifacts in SRI. One potentially powerful tool is the magnitude of the correlation coefficient. The correlation coefficient is computed for every pixel in the image as part of two-dimensional phase-sensitive speckle tracking. If a robust, two-dimensional search is performed, then the primary cause of speckle decorrelation is the strain magnitude [16]. A trashogram, defined as $1 - |\rho|$, where $|\rho|$ is the magnitude of the correlation coefficient, can identify regions of high and low strain magnitude. A trashogram for the present simulation is presented in Fig. 5(c) over a unipolar gray scale from 0.00 to 0.02. Note that it identifies regions of high deformation magnitude.

For this particular scan geometry and deformation pattern, the trashogram shows more angle dependence than either $|\varepsilon|$ or $|\nabla v|$, but it still provides valuable information confirming other strain magnitude measures, as experimentally demonstrated subsequently. Note that areas of slightly higher decorrelation correspond to positions where the displacement vector is at an angle of 45° with respect to the ultrasound propagation direction. This condition is the poorest for lateral estimation, producing a slightly heightened trashogram in these regions. Images such as those in Fig. 5 can be combined to produce robust images of deformation magnitude, relatively free of angle-dependent artifacts.

B. Measurements

The axial displacement measured in the rubber phantom at the frame corresponding to maximum compression is presented in Fig. 6(a) over a bipolar gray scale representing an interframe displacement of -87.5 μm (black) to 87.5 μm (white). Again, a plus sign corresponds to motion away from the transducer (down), and a minus sign rep-

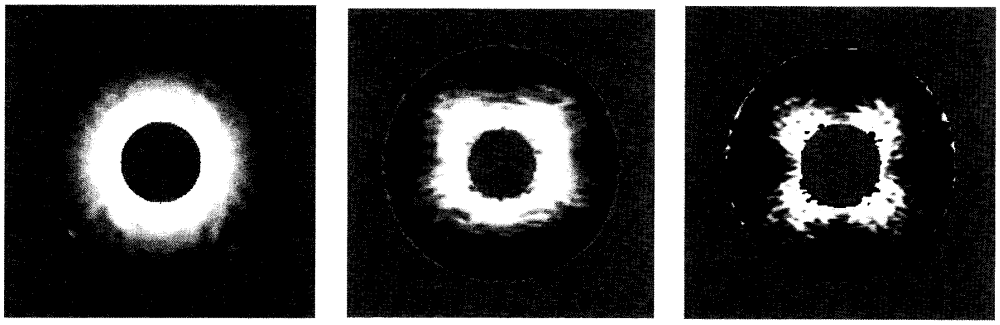

Fig. 5. a) Magnitude of the gradient of the axial displacement in the simulated annular phantom displayed over a unipolar gray scale, where white represents a deformation rate of 1.0 s^{-1} and black represents zero deformation; b) strain magnitude using all spatial derivatives of the full two-dimensional displacement vector displayed over the same gray scale as panel (a); and c) trashogram $(1- \mid \rho \mid)$ in the simulated annular phantom displayed over a unipolar gray scale from 0.0 to 0.02.

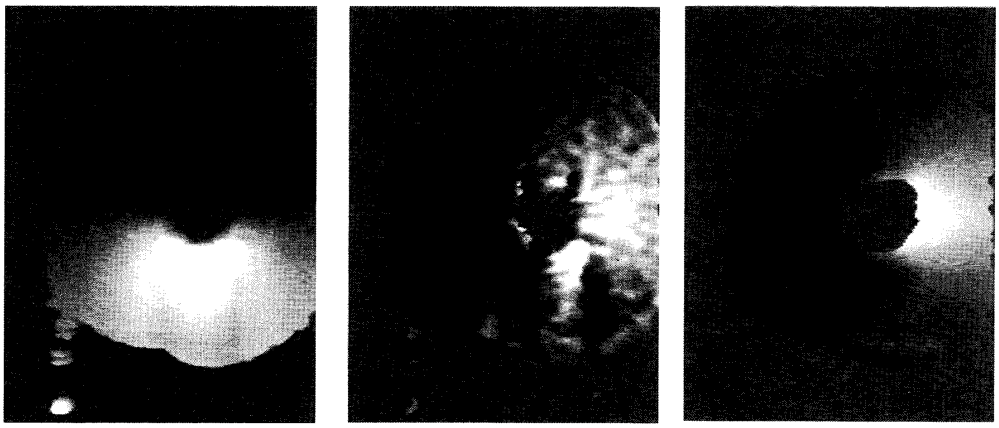

Fig. 6. Displacements measured in thick-walled tube phantom for frame corresponding to maximum compression. a) Interframe axial displacement, where white represents a downward displacement of 87.5 μm and black represents an upward displacement of 87.5 μm; b) lateral displacement, where white represents a rightward displacement of 87.5 μm and black represents a leftward displacement of 87.5 μm; and c) lateral displacement resulting from incompressibility processing of panel (b) based on the axial displacement of panel (a) using the same gray scale as panel (b).

resents motion toward the transducer (up). Note that the axial displacement near 3 o'clock and 9 o'clock is nearly zero, even though there is significant radial displacement in these regions.

The estimated lateral displacement over precisely the same display dynamic range is presented in Fig. 6(b), where a plus sign corresponds to motion to the right and a minus sign represents motion to the left. Again, the lateral displacement is significantly noisier than the axial. The result of incompressibility processing using both axial and lateral displacement estimates produces the lateral displacement map of Fig. 6(c). Note the higher SNR for this image [Fig. 6(c)] compared with that produced directly by the speckle tracking procedure [Fig. 6(b)].

The two components of the axial displacement gradient for this frame are presented in Fig. 7(a) (axial component) and Fig. 7(b) (lateral component) over the same display dynamic range using a bipolar gray scale, with black denoting compression and white denoting expansion. The dynamic range for this display represents a peak strain rate magnitude of 1 s^{-1} (i.e., the gray scale spans a strain rate of ± 1 s^{-1}). The same artifacts observed in the simulation are present in this image. There is a hint of an altered deformation pattern near the inclusion between 11 and 1 o'clock, but there are also other apparent low deformation regions throughout both images.

The magnitude of the axial displacement gradient is presented in Fig. 8(a) over a unipolar gray scale, where black represents a strain rate of 0.15 s^{-1} and white corresponds to a strain rate of 1.0 s^{-1}. Reduced deformation magnitude is clearly seen in the inclusion neighborhood centered at 12 o'clock. There also appears to be reduced deformation magnitude near 5 o'clock and 7 o'clock. Similarly, the strain magnitude is presented over precisely the same display dynamic range in Fig. 8(b). This image shows all of the same features as the $|\nabla v|$ one but at slightly lower spatial resolution. To corroborate these estimates, they were compared with the trashogram $(1 - |\rho|)$, presented in Fig. 8(c) on a unipolar gray scale over a display dynamic range of 0.0 to 0.07. The apparent low defor-

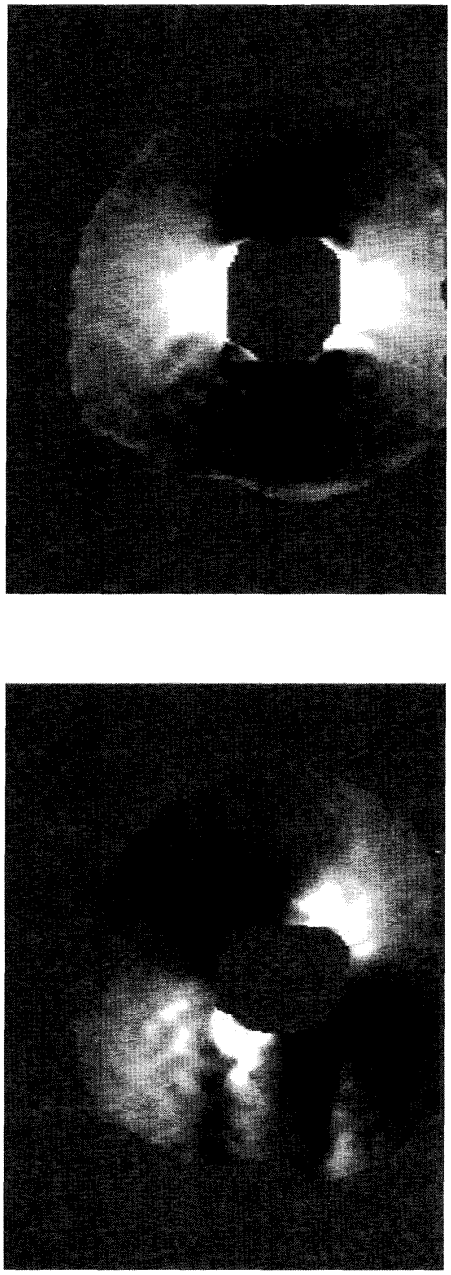

Fig. 7. Two components of the measured gradient of the axial displacement in thick-walled tube phantom for frame corresponding to maximum compression. a) Axial component of gradient with a bipolar gray scale, where black represents a compression rate of 1.0 s^{-1} and white represents an expansion rate of 1.0 s^{-1}; b) lateral component of gradient using the same gray scale.

mation regions near 5 o'clock and 7 o'clock are in areas of high "trash." This is an inconsistent result, identifying these regions as artifacts.

An inspection of the B-scan movie for this experiment clearly exhibits refraction effects in these areas because of the relatively large sound velocity mismatch between room temperature water pressurizing the phantom lumen and the rubber constituting the phantom host material. Other regions in the image are well correlated, however, indicating that the low deformation magnitude at about 12 o'clock near the phantom outer surface is real. Consequently, by combining strain magnitude and trashogram information, it may be possible to identify the hard inclusion. Considering that the inclusion is only a few millimeters thick and that the elastic modulus contrast is only a factor of three, this is a significant result.

Fig. 9 and 10 present one possible display format to identify non-deforming tissue. First, the mean strain magnitude (or $|\nabla v|$) in each frame of the sequence was computed, and the strain magnitude relative to the mean was obtained in every pixel. The relative strain magnitude and trashogram values at each pixel for every frame were compared with a threshold. Deformation data were retained if and only if the relative strain magnitude was below a threshold (relative strain magnitude threshold = 0.6) and the correlation coefficient was simultaneously above a different threshold (correlation coefficient threshold = 0.985). For all pixels satisfying the dual threshold test, the relative strain magnitude was encoded on a negative hot color scale from a relative magnitude of 0.85 to 0.0 (i.e., the least deforming tissue was the "hottest" on the display because a strain magnitude of zero represents no deformation). These color-encoded pixels were then superimposed on the original B-scan image for every frame in the sequence. For those frames in which the average strain magnitude was close to zero, no pixels were colored, and only the B-scan was presented.

The image of Fig. 9(a) is the result of this processing for the image frame corresponding to Fig. 6 through 8 using $|\nabla v|$ as the estimated deformation magnitude. The same image is recomputed in Fig. 9(b) using $|\varepsilon|$ as the estimated deformation magnitude. Although the processing steps appear complicated, they are actually quite simple and can identify non-deforming tissue. In Fig. 10, the result of the same processing using precisely the same parameters is presented for the phantom rotated by 90 degrees, where again panel (a) uses $|\nabla v|$ as the estimated deformation magnitude and panel (b) uses $|\varepsilon|$ as the estimated deformation magnitude. Clearly, the non-deforming region is also rotated by 90 degrees. Note that there are artifacts in several regions of these images near the phantom outer surface, where the overall deformation magnitude is lower than the mean. Artifacts appear to be slightly reduced, and the inclusion region is slightly better defined, in images using $|\varepsilon|$ as the estimated deformation magnitude. In any event, these artifacts can be easily identified in the movies for all image frames presented at the web site http://bul.eecs.umich.edu/research/intracardiac/index.

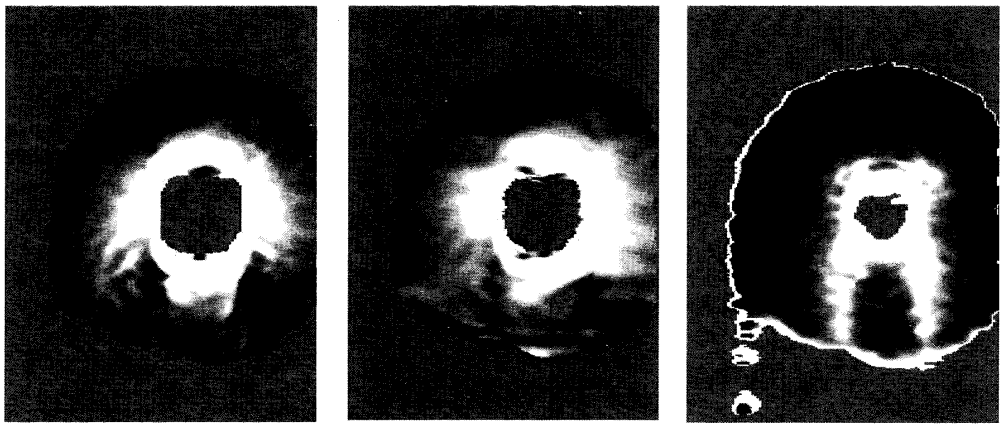

Fig. 8. a) Magnitude of the gradient of the axial displacement measured in the thick-walled tube phantom for frame corresponding to maximum compression over a unipolar gray scale, where white represents a deformation rate of 1.0 s^{-1} and black represents a deformation rate of 0.15 s^{-1}; b) strain magnitude using all spatial derivatives of the full two-dimensional displacement vector displayed over the same gray scale as panel (a); and c) trashogram $(1-|\rho|)$ for the same conditions displayed over a unipolar gray scale from 0.0 to 0.07.

html. There are only about 60 frames in each of these movies. They have simply been time(frame) averaged and decimated from the original 166 frame sequence. The smoothly varying non-deforming inclusions are easily distinguishable from noisy boundary artifacts in these movies.

IV. Discussion and Summary

The results of both simulations and experiments on model systems show that SRI have the potential to clearly identify non-deforming regions of a periodically deforming, continuous medium. Strain magnitude maps, combined with other correlation measures, such as the trashogram, can greatly reduce angle-dependent artifacts and complement conventional TVI and SRI displays. Combinations of these measures can be a potentially valuable tool set to identify deformation anomalies in the heart. In general, two-dimensional phase-sensitive speckle tracking should be applicable to functional imaging of the heart if images can be captured fast enough to track propagation of mechanical contractions along the cardiac wall.

The magnitude of the gradient of one component of the displacement eliminated angle-dependent artifacts because it equals the strain magnitude for the simple two-dimensional system considered here. This will not be the case for general three-dimensional deformations. Images of the strain magnitude derived from the full three-dimensional strain tensor will not exhibit angle-dependent artifacts. Lower dimension approximations certainly will produce some artifacts in describing full three-dimensional deformations. Nevertheless, two-dimensional strain magnitude maps based on the estimated two-dimensional displacement vector should be much closer to the true deformation magnitude than current SRI estimates based on tissue Doppler systems.

In addition to the displacement along the propagation direction, two-dimensional speckle tracking estimates both the magnitude of the correlation coefficient and the lateral displacement (i.e., displacement orthogonal to the ultrasound propagation direction) at every pixel in the image. The trashogram is derived from spatial maps of the correlation coefficient. As demonstrated in this study, it can identify artifacts in estimated deformation patterns. This will be even more important to accurately characterize three-dimensional deformation fields using two-dimensional images.

In a zero-dimensional search (i.e., traditional Doppler measurement), decorrelation is produced by both deformation and displacement in any direction. For a one-dimensional search (i.e., one-dimensional speckle tracking along an RF A-line), decorrelation results from both total deformation and displacement in any of two directions. A full two-dimensional search reduces decorrelation effects to true deformations and motion in only one direction (i.e., displacement out of the scan plane). Finally, the correlation coefficient is reduced from unity only by deformations for a true, three-dimensional search. By increasing the search dimension, the trashogram more closely correlates with the deformation magnitude.

The trashogram produced by a robust, two-dimensional speckle tracking algorithm is a potentially invaluable tool for SRI in two ways. First, real-time presentation of the trashogram can help the operator identify periods of the cardiac cycle in which the deformation is primarily in-plane for a particular scan orientation. Over those periods, two-dimensional speckle tracking results can well characterize true tissue deformations. And second, the trashogram can corroborate strain magnitude measures estimated from spatial derivatives of the in-plane displacement. As noted previously, non-deforming regions must have both low strain magnitude and a high correlation coefficient (i.e., low trash).

Incompressibility processing greatly improved lateral displacement estimates needed for strain magnitude computations. The specific form of incompressibility process-

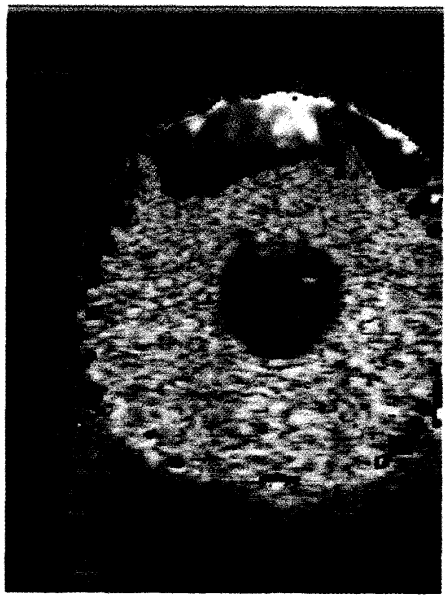

(a)

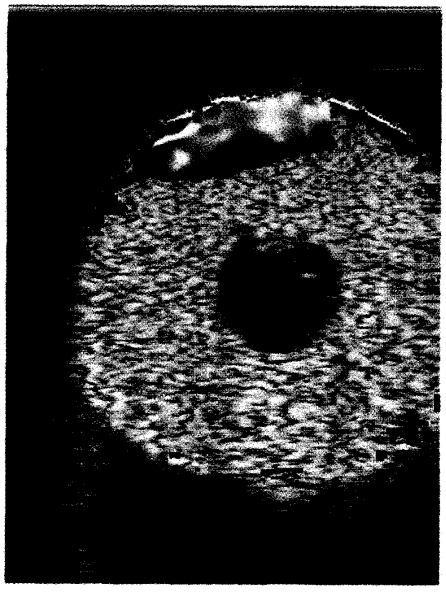

(b)

Fig. 9. Non-deforming regions of thick-walled tube phantom for the frame corresponding to maximum compression are color-coded and superimposed on the B-scan for the case in which the hard inclusion is near the top. a) Deformation based on magnitude of axial displacement gradient and b) deformation based on strain magnitude using spatial derivatives of the full two-dimensional displacement vector.

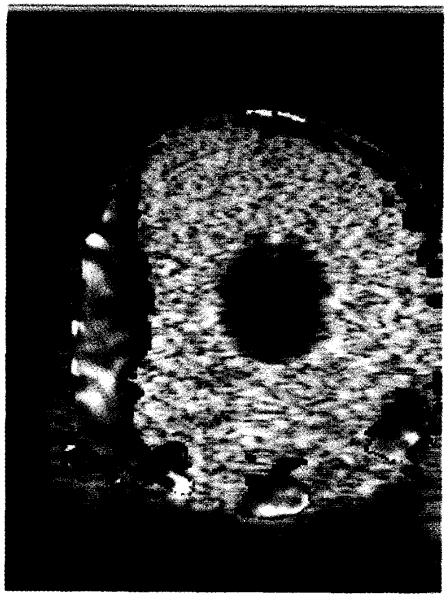

(a)

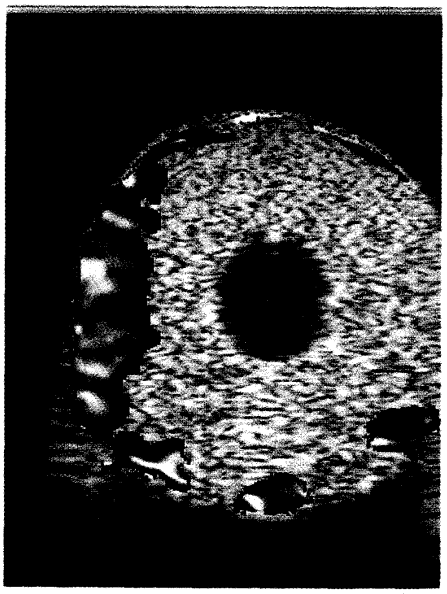

(b)

Fig. 10. Non-deforming regions of thick-walled tube phantom for the frame corresponding to maximum compression are color-coded and superimposed on the B-scan for the case in which the hard inclusion is near the left side. a) Deformation based on magnitude of axial displacement gradient and b) deformation based on strain magnitude using spatial derivatives of the full two-dimensional displacement vector.

ing used here is accurate only if the mechanical system can be well modeled as a plane strain state (i.e., two-dimensional mechanical system) [30]–31]. Cardiac deformations certainly cannot be generally modeled as a two-dimensional mechanical system. Consequently, these methods will not always be accurate for general cardiac deformations imaged by a two-dimensional scanner. However, over periods of the heart cycle in which deformations are primarily in-plane, as judged by the trashogram, incompressibility methods can be applied. This will produce more accurate estimates of the in-plane strain magnitude than the magnitude of the gradient of just one displacement component. The validity of incompressibility methods for two-dimensional imaging of cardiac deformations will be the subject of future clinical investigations.

There are two significant technical hurdles that must be addressed before two-dimensional phase-sensitive speckle tracking can be directly applied to functional imaging of the heart. First, a real-time correlation processor must be designed and built to operate at the very high frame rates demanded by this application. Based on the current state of the art in microcomputers and field programmable gate arrays (FPGA), we believe this is a very solvable problem in the immediate future.

Second, high quality two-dimensional, and ultimately three-dimensional, images must be produced at high frame rates. The propagation time of the mechanical wave in the left ventricle from base to apex during systole is, on average, about 55 ms for the adult human heart [6]. To fully capture the details of wave propagation through the left ventricle using two-dimensional phase-sensitive speckle tracking, this means full frame images of the ventricle must be acquired in 4 to 5 ms, representing frame rates of 200 to 250 Hz. This is certainly an achievable rate at low spatial resolution, but is at the edge of current technology for high spatial resolution images.

One possible solution to the frame rate problem is an intracardiac array [36]. Intracardiac arrays can greatly reduce the propagation distance from the transducer to the cardiac wall, permitting high pulse repetition rates with concomitant high frame rates. Because higher operating frequencies can also be used compared with conventional echocardiography, these arrays may be able to produce very high resolution images. Coupling TVI and SRI derived from two-dimensional phase-sensitive speckle tracking with these arrays is an exciting prospect for functional imaging of the heart.

In summary, two-dimensional phase-sensitive speckle tracking has been proposed as an alternate to Doppler methods for SRI of the heart. The results of simulations and experiments on a simple two-dimensional model of cardiac deformations demonstrate that high spatial resolution images of the strain magnitude can identify non-deforming regions. The proposed methods should complement current TVI and SRI methods for functional imaging of cardiac mechanics.

ACKNOWLEDGMENTS

We thank Ramon Erkamp and Takashi Buma for invaluable technical support. Use of an Ultramark 9 scanner by ATL is also gratefully acknowledged.

REFERENCES

[1] W. M. McDicken, G. R. Sutherland, C. M. Moran, and L. N. Gordon, "Colour Doppler velocity imaging of the myocardium," *Ultrasound Med. Biol.*, vol. 18, no. 61, pp. 651–654, 1992.

[2] G. R. Sutherland, M. J. Stewart, and K. W. E. Groundstroem, "Color Doppler myocardial imaging: A new technique for assessment of myocardial function," *J. Amer. Soc. Echocardiogr.*, vol. 7, pp. 441–458, Sep.–Oct. 1994.

[3] D. Fleming, X. Xia, W. M. McDicken, G. R. Sutherland, and L. Fenn, "Myocardial velocity gradients detected by Doppler imaging," *Br. J. Radiol.*, vol. 67, pp. 679–688, Jul. 1994.

[4] M. Uematsu, K. Miyatake, N. Tanaka, H. Matsuda, A. Sano, N. Yamazaki, M. Hirama, and M. Yamagishi, "Myocardial velocity gradient as a new indicator of regional left ventricular contraction: Detection by a two-dimensional tissue Doppler imaging technique," *J. Amer. Coll. Cardiol.*, vol. 26, no. 1, pp. 217–223, Jul. 1995.

[5] P. Palka, A. Lange, A. D. Fleming, J. E. Donnelly, D. P. Dutka, I. R. Starkey, T. R. D. Shaw, G. R. Sutherland, and K. A. A. Fox, "Differences in myocardial velocity gradient measured throughout the cardiac cycle in patients with hypertrophic cardiomyopathy, athletes and patients with left ventricular hypertrophy due to hypertension," *J. Amer. Coll. Cardiol.*, vol. 30, pp. 760–768, Sep. 1997.

[6] A. Heimdal, A. Stoylen, H. Torp, and T. Skjaerpe, "Real-time strain rate imaging of the left ventricle by ultrasound," *J. Amer. Soc. Echocardiogr.*, vol. 11, pp. 1013–1019, Nov. 1998.

[7] H. Tsutsui, M. Uematsu, H. Shimizu, M. Yamagishi, N. Tanaka, H. Matsuda, and K. Miyatake, "Comparative usefulness of myocardial velocity gradient in detecting ischemic myocardium by a dobutamine challenge," *J. Amer. Coll. Cardiol.*, vol. 31, pp. 89–93, Jan. 1998.

[8] A. Stoylen, A. Heimdal, K. Bjornstad, H. Torp, and T. Skjaerpe, "Strain imaging by ultrasound in the diagnosis of regional dysfunction of the left ventricle," *Echocardiography*, vol. 16, no. 4, pp. 323–329, 1999.

[9] J. U. Voigt, M. F. Arnold, M. Karlsson, L. Hubbert, T. Kukulski, L. Hatle, and G. R. Sutherland, "Assessment of regional longitudinal myocardial strain rate derived from Doppler myocardial imaging indices in normal and infarcted myocardium," *J. Amer. Soc. Echocardiogr.*, vol. 13, pp. 588–598, Jun. 2000.

[10] A. Heimdal, T. Abraham, C. Pislaru, and M. Belohlavek, "Angle dependency of strain rate imaging in an animal model," *J. Amer. Soc. Echocardiogr.*, vol. 13, p. 484, 2000.

[11] P. L. Castro, N. L. Greenberg, J. Drinko, M. J. Garcia, and J. D. Thomas, "Potential pitfalls of strain rate imaging: Angle dependency," *Biomed. Sci. Instrum.*, vol. 36, pp. 197–202, 2000.

[12] M. O'Donnell, A. R. Skovoroda, and B. M. Shapo, "Measurement of wall motion using Fourier based speckle tracking algorithms," in *Proc. 1991 IEEE Ultrason. Symp.*, pp. 1101–1104.

[13] M. O'Donnell, S. Y. Emelianov, A. R. Skovoroda, M. A. Lubinski, and B. M. Shapo, "Quantitative elasticity imaging," in *Proc. 1993 IEEE Ultrason. Symp.*, pp. 893–903.

[14] M. O'Donnell, A. R. Skovoroda, B. M. Shapo, and S. Y. Emelianov, "Internal displacement and strain imaging using ultrasonic speckle tracking," *IEEE Trans. Ultrason., Ferroelect., Freq. Contr.*, vol. 41, pp. 314–325, May 1994.

[15] M. A. Lubinski, S. Y. Emelianov, and M. O'Donnell, "Speckle tracking methods for ultrasonic elasticity imaging using short time correlation," *IEEE Trans. Ultrason., Ferroelect., Freq. Contr.*, vol. 46, pp. 82–96, Jan. 1999.

[16] ——, "Adaptive strain estimation using retrospective processing," *IEEE Trans. Ultrason., Ferroelect., Freq. Contr.*, vol. 46, pp. 97–107, Jan. 1999.

[17] D. P. Shattuck, M. D. Weinshenker, S. W. Smith, and O. T. von Ramm, "Explososcan: A parallel processing technique for high

speed ultrasound imaging with linear phased arrays," *J. Acoust. Soc. Amer.*, vol. 75, pp. 1273–1282, Apr. 1984.
[18] H. F. Fidel, "Parallel processing of simultaneous ultrasound vectors," U.S. Patent 4622634, November 11, 1986.
[19] L. J. Augustine, "High resolution multiline ultrasonic beamformer," U.S. Patent 4644795, February 24, 1987.
[20] M. O'Donnell, "Method of, and apparatus for, obtaining a plurality of different return energy beams responsive to a single excitation event," U.S. Patent 4886069, December 12, 1989.
[21] ——, "Efficient parallel receive beam forming for phased array imaging using phase rotation," in *Proc. 1990 IEEE Ultrason. Symp.*, pp. 1495–1498.
[22] O. T. von Ramm, S. W. Smith, and H. G. Pavy, "High-speed ultrasound volumetric imaging system—Part II: Parallel processing and image display," *IEEE Trans. Ultrason., Ferroelect., Freq. Contr.*, vol. 38, pp. 109–115, 1991.
[23] M. O'Donnell, "Ultrasonic imaging systems with multiple, dynamically focused transmit beams," U.S. Patent 5142649, August 25, 1992.
[24] K. Okada, A. Sasaki, and M. Yoshida, "Ultrasonic diagnostic apparatus capable of performing switching between single beam reception and simultaneous parallel beam reception," U.S. Patent 5351690, October 4, 1994.
[25] H. Fukukita, L. X. Yao, Z. Banjanin, J. Kim, H. Hagiwara, and M. Kawabuchi, "Digital beamformer having multi-phase parallel processing," U.S. Patent 5369624, November 29, 1994.
[26] T. J. Hunt, B. M. Herrick, K. K. Robertson, K. E. Thiele, and J. M. Ziel, "Ultrasound imaging system using line splicing and parallel receive beam formation," U.S. Patent 5462057, October 31, 1995.
[27] J. Shen and E. S. Ebbini, "A new coded-excitation ultrasound imaging system—Part I: Basic principles," *IEEE Trans. Ultrason., Ferroelect., Freq. Contr.*, vol. 43, pp. 131–140, Jan. 1996.
[28] J. Y. Lu, "2D and 3D high frame rate imaging with limited diffraction beams," *IEEE Trans. Ultrason., Ferroelect., Freq. Contr.*, vol. 44, pp. 839–856, Jul. 1997.
[29] N. J. Wright, C. R. Cole, and A. Gee, "Method and apparatus for receive beamformer system," U.S. Patent 6042547, March 28, 2000.
[30] M. A. Lubinski, S. Y. Emelianov, K. R. Raghavan, A. E. Yagle, A. R. Skovoroda, and M. O'Donnell, "Lateral displacement estimation using tissue incompressibility," *IEEE Trans. Ultrason., Ferroelect., Freq. Contr.*, vol. 43, pp. 247–256, Mar. 1996.
[31] A. R. Skovoroda, M. A. Lubinski, S. Y. Emelianov, and M. O'Donnell, "Nonlinear estimation of lateral displacement using tissue incompressibility," *IEEE Trans. Ultrason., Ferroelect., Freq. Contr.*, vol. 45, pp. 491–503, Mar. 1998.
[32] P. C. Li and M. O'Donnell, "Elevational spatial compounding," *Ultrason. Imaging*, vol. 16, pp. 176–189, 1994.
[33] ——, "Phase aberration correction on two-dimensional conformal arrays," *IEEE Trans. Ultrason., Ferroelect., Freq. Contr.*, vol. 42, pp. 73–82, Jan. 1995.
[34] S. Krishnan and M. O'Donnell, "Transmit aperture processing for non-linear contrast agent imaging," *Ultrason. Imaging*, vol. 18, pp. 77–105, 1996.
[35] R. Q. Erkamp, P. Wiggins, A. R. Skovoroda, S. Y. Emelianov, and M. O'Donnell, "Measuring the elastic modulus of small tissue samples," *Ultrason. Imaging*, vol. 20, pp. 17–28, Jun. 1998.
[36] J. B. Seward, D. L. Packer, R. C. Chan, M. Curley, and A. J. Tajik, "Ultrasound cardioscopy: Embarking on a new journey," *Mayo Clin. Proc.*, vol. 71, pp. 629–635, Jul. 1996.

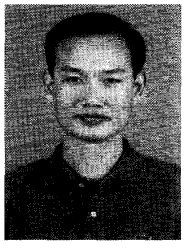

Xunchang Chen graduated with a BS degree in biomedical instrumentation from Shanghai Jiaotong University, Shanghai, China in 1993 and received his MS degree in biomedical engineering from Virginia Commonwealth University, Richmond, VA in 1998. He is currently pursuing the Ph.D. degree in biomedical engineering at University of Michigan, Ann Arbor, MI. His current interests include elasticity imaging, signal/imaging processing, and ultrasonic imaging simulations.

Stanislav Y. Emelianov (M'94) was born in May 1966. He received the B.S. and M.S. degrees in physics in 1986 and 1989, respectively, from Moscow State University, and the Institute of Mathematical Problems of Biology of the Russian Academy of Sciences, Russia.

In 1989, he joined the Institute of Mathematical Problems of Biology, where he was engaged in both mathematical modeling of soft tissue biomechanics and experimental studies of noninvasive methods in medical diagnostics based on tissue elasticity variations. Following his graduate work, he moved to the University of Michigan, Ann Arbor, as a post-doctoral fellow in the Electrical Engineering and Computer Science Department working on applications of imaging systems for medical diagnosis and nondestructive testing. Dr. Emelianov is currently a research scientist in the Biomedical Ultrasonics Laboratory at the University of Michigan and involved primarily in the theoretical and practical aspects of ultrasound elasticity imaging. He is the author of several scientific papers. His research interests are in the areas of tissue biomechanics, medical imaging systems, and nondestructive material testing.

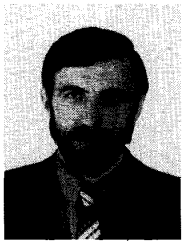

Andrei R. Skovoroda received the B.S. and M.S. degrees in mathematics and mechanics in 1973 and 1975, respectively, from the Novosibirsk State University, USSR, and the Ph.D. degree in 1985 from the Moscow State University, USSR.

From 1975 to 1977 he was a lecturer in theoretical mechanics at the College of Textile Technology, Barnaul, USSR. From 1977 to 1980 he was a Ph.D. researcher at the subfaculty of Plasticity of the Moscow State University, where he worked on the dynamic behavior of plates under blast-type loading. In 1981 he held an appointment as a junior research associate at the Laboratory of Mathematical Modeling of the Research Computing Center of the USSR Academy of Sciences (the present name: Institute of Mathematical Problems of Biology, Russian Academy of Sciences), where he developed efficient mathematical methods to solve the differential equations of the theory of elasticity. In 1986 he became a senior research associate and was scientific secretary at the same institute from 1988 to 1993. He is currently head of the Laboratory of Mathematical Problems in Biomechanics and works on the biomechanics of soft tissue.

Dr. Skovoroda has authored and co-authored more than 90 articles for archival publications and papers presented at all-union and international meetings.

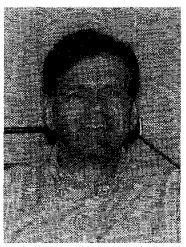

Matthew O'Donnell (M'79–SM'84–F'93) has a B.S. and Ph.D. in Physics from the University of Notre Dame (1972 and 1976, respectively). Following his graduate work, Dr. O'Donnell moved to Washington University in St. Louis as a postdoctoral fellow in the Physics Department, working on applications of ultrasonics to medicine and non-destructive testing. He subsequently held a joint appointment as a Senior Research Associate in the Physics Department and a Research Instructor of Medicine in the Department of Medicine at Washington University. In 1980, he moved to General Electric Corporate Research and Development Center in Schenectady, New York, where he continued to work on medical electronics, including MRI and ultrasound imaging systems. During the 1984 and 1985 academic year, he was a visiting fellow in the Department of Electrical Engineering at Yale University, investigating automated image analysis systems. In a bold move during 1990, Dr. O'Donnell became Professor of Electrical Engineering & Computer Science at the University of Michigan in Ann Arbor, Michigan. Since 1997, he's held a

joint appointment as Professor of Biomedical Engineering at Michigan, and, in 1998, he was named the Jerry W. and Carol L. Levin Professor of Engineering. Currently, he is the Chair of the Biomedical Engineering Department. His most recent work has explored new imaging modalities in biomedicine, including elasticity imaging, in vivo microscopy, and catheter-based devices.

Dr. O'Donnell is a member of Sigma Xi, the American Physical Society, and is a fellow of both the IEEE and the AIMBE. He has authored or coauthored over 140 archival publications, including two that received best paper awards. He has had numerous presentations at national meeetings and holds 40 patents.